# The $Ni^{1+\delta}$ metallic state and purely Ni-$d_{x^2-y^2}$-occupied Fermi surface in the $SrNiO_2$-based superlattice at ambient pressure

Miao Li,[1,2,*] Zhenyu Ding,[1,2,*] Yuqiang Liu,[1,2] Liangyu Li,[1,2] Gang Wu,[3,†] and Xiaoping Yang[1,2,‡]

[1]*High Magnetic Field Laboratory, HFIPS, Chinese Academy of Sciences, Hefei 230031, China*
[2]*Science Island Branch of Graduate School, University of Science and Technology of China, Hefei 230026, China*
[3]*Materials Science and Chemistry, Institute of High Performance Computing, 1 Fusionopolis Way, 16-16 Connexis, Singapore 138632, Singapore*

(Dated: March 21, 2025)

The rich physics of nickelates has garnered widespread attention, particularly for their superconductivity and the prominent Ni-$d_{x^2-y^2}$ dominated Fermi surface. Motivated by the $Ni^{1+\delta}$ superconductivity in infinite-layer $NdNiO_2$ ($T_c$ = 15 K) and high-pressure superconducting $La_3Ni_2O_7$ ($T_c$ = 80 K), we designed a $(SrNiO_2)_2/(LaTiO_3)_1$ superlattice with a two-dimensional confined bi-layer $NiO_2$. $LaTiO_3$ acts as an electron donor, transferring a full electron to the $NiO_2$ double layers due to the electronegativity difference between Ni(1.91) and Ti(1.54). This charge transfer transforms the Fermi surface from a multi-orbital character, resembling that of $NdNiO_2$, into one dominated purely by $Ni^{1+\delta}$-$d_{x^2-y^2}$ orbitals. Factors that limited the transition temperature in $NdNiO_2$, such as 5*d*-3*d* hybridization, self-doping between Nd and Ni atoms, and the weak *p*-*d* hybridization between Ni and O atoms, are effectively suppressed and enhanced, respectively. The nearest-neighbor $e_g$ hoppings closely resemble those in undoped infinite-layer $NdNiO_2$, though they are smaller than those found in high-pressure $La_3Ni_2O_7$. Similar to $La_3Ni_2O_7$, this superlattice exhibits a low-spin magnetic state with instability stemming from nearly degenerate magnetic ground states. Additionally, F-doping in $NiO_2$ double layers can be used to fine-tune the Ni valence state and the magnetic coupling, simulating the effects of oxygen pressure in the preparation. Our research offers new insights into the mechanisms driving high-$T_c$ superconductivity in nickelates under ambient pressure, emphasizing the pivotal role of heterostructure engineering in these processes.

## I. INTRODUCTION

Since the discovery of high-transition-temperature (high-$T_c$) cuprate superconductors in 1986, there has been a persistent effort to uncover similar phenomena in nickelates [1–17]. Over the past decade, numerous experiments have sought to manipulate the electronic structure of $d^7$-$Ni^{3+}$ oxides to achieve superconductivity [9, 11, 12]. However, no $Ni^{3+}$ superconductors have been experimentally realized. A fundamental reason, as highlighted by Hwang, is the lack of full $Ni^{3+}$-$e_g^1$ orbital polarization [4], i.e. half-occupied Ni-$d_{x^2-y^2}$ orbital and Fermi surface.

Although the $Ni^{1+}$ valence state does not naturally occur, theoretical predictions of superconductivity in $Ni^{1+}$ nickelates such as $RNiO_2$ (*R* = La, Nd, Sm, etc.) date back to 1999 [9, 13], primarily due to their similar $d^9$ electronic configuration and planar $NiO_2$ square lattice, reminiscent of $Cu^{2+}$ in cuprates. In 2019, Li et al. successfully synthesized the $Ni^{1+\delta}$ infinite-layer superconducting film $Nd_{0.8}Sr_{0.2}NiO_2$ ($T_c$ = 15 K) using $CaH_2$ chemical reduction [4]. This was followed by the synthesis of $Pr_{0.82}Sr_{0.18}NiO_2$, which exhibited a maximum $T_c$ of 31 K under 12.1 GPa [18], though still below the McMillan limit of 40 K [19]. The low superconducting transition temperature in $Ni^{1+}$ nickelates could be attributed to *d*-*d* orbital hybridization and self-doping between 5*d*-*R* atoms and 3*d*-Ni atoms, which lead to a multi-orbital Fermi surface, poor nesting, and the absence of a Mott-insulating state [4, 7, 8, 20]. Moreover, unlike cuprates, weak antiferromagnetic (AFM) coupling [20, 21] and an increase in charge transfer energy between the *d* and *p* orbitals have been observed in $RNiO_2$. This increase diminishes the Zhang-Rice effect [7, 21–23].

Recently, in $La_3Ni_2O_7$ single crystals with an average Ni valence of $Ni^{2.5+}$ ($3d^{7.5}$), Sun et al. reported a superconducting transition temperature as high as 80 K under 14 GPa [24]. At ambient pressure, $La_3Ni_2O_7$ shows a charge density wave (CDW) instability [25, 26], which vanishes as pressure increases, accompanied by a structural transition from *Amam* to *Fmmm*. Furthermore, the Ni-$d_{3z^2-1}$ orbitals between the double layers form dimers [24, 27, 28], creating occupied bonding and unoccupied anti-bonding states. Consequently, the Fermi surface becomes dominated by the Ni-$d_{x^2-y^2}$ orbital. While the self-doping mechanism in nickelates is distinct from that in cuprates, where electrons rearrange between Ni-$d_{3z^2-1}$ and Ni-$d_{x^2-y^2}$ orbitals under pressure, this highlights the unique potential nickelates offer for advancing our understanding of high-$T_c$ superconductivity.

Beyond cation doping in cuprates and $Ni^{1+}$ nickelates, and pressure-induced self-doping in $La_3Ni_2O_7$, oxide heterostructures have been extensively explored over the past decade as a means of tuning the physical properties of oxides [29–34] at ambient pressure. In this study, we focus on $SrNiO_2$, a layered material with a $Ni^{2+}$-$d^8$ electronic configuration and a planar $NiO_2$ square lattice. By combining $SrNiO_2$ with $LaTiO_3$, we constructed $(SrNiO_2)_n/(LaTiO_3)_1$ superlattices ($(SNO)_n/(LTO)_1$ SLs) with $n = 1, 2$, modulating the electronic structure of the $NiO_2$ planes. For $n = 2$, an integer charge transfer occurs: $2Ni^{2+}/Ti^{3+} \rightarrow (Ni^{1.41+}+Ni^{1.59+})/Ti^{4+}$, resulting in a Fermi surface dominated only by the Ni-$d_{x^2-y^2}$ or-

* These author contributed equally to this work.
† wug@ihpc.a-star.edu.sg
‡ xpyang@hmfl.ac.cn

bital, similar to that found in cuprates. Compared to infinite-layer $Ni^{1+\delta}$ nickelate films like $Nd_{0.8}Sr_{0.2}NiO_2$, the detrimental effects on superconductivity, such as 5*d*-3*d* hybridization and self-doping between Nd and Ni, as well as weak *p*-*d* hybridization between Ni and O atoms, have been fully mitigated and improved, respectively. The nearest-neighbor $e_g$ hopping parameters in $(SNO)_2/(LTO)_1$ closely align with those in infinite-layer $RNiO_2$, and are smaller than those reported in high-pressure $La_3Ni_2O_7$ [35], due to differences in Ni valence state and pressure-induced structural changes. Magnetic state calculations reveal a low-spin state with magnetic instability at a reasonable correlation $U$ value of 1 to 3 eV, similar to what is observed in $La_3Ni_2O_7$. The magnetic coupling, sensitive to Ni valence states, can be fine-tuned by F-doping to mimic oxygen pressure environments during the preparation process.

## II. COMPUTATIONAL DETAILS

We performed density functional theory (DFT) calculations using a plane-wave basis and the projector augmented-wave (PAW) method [36, 37], as implemented in the Vienna *ab* initio Simulation Package (VASP) [38, 39]. The Perdew-Burke-Ernzerhof (PBE) exchange-correlation functional was applied within the generalized gradient approximation (GGA) framework [40–42]. A plane wave cutoff energy of 600 eV was employed, and $k$-point sampling was carried out using the Monkhorst-Pack method with a $k$-point spacing of 0.02 $Å^{-1}$. Lattice constants along the $z$-direction and atomic internal positions were optimized using the conjugate gradient technique, ensuring that no atomic force exceeded 0.01 eV/Å in the final structures. For the DFT GGA+$U$ magnetic calculations, the Ni-3*d* on-site Coulomb interaction was accounted for using a $J/U$ ratio of 0.2, a typical value for the 3*d*-transition metals, based on the rotationally invariant Liechtenstein DFT+$U$ formulation [43] implemented in the VASP code. Additionally, to gain insight into the microscopic Ni-3*d* orbital physics of system, we applied the maximally localized Wannier functions (MLWFs) method to fit the Ni-3*d* GGA bands and extract model Hamiltonian parameters, utilizing the WANNIER90 package [44, 45].

The generalized DFT+$U$ functional is the following [43]:

$$E^{\mathrm{DFT}+U}[\rho^{\sigma}(r),\{n^{\sigma}\}] = E^{\mathrm{DFT}}[\rho^{\sigma}(r)] + E^{U}[\{n^{\sigma}\}] - E_{\mathrm{dc}}[\{n^{\sigma}\}] \quad (1)$$

where $\rho^{\sigma}(r)$ is the charge density for electrons with spin projection $\sigma$, while $\{n^{\sigma}\}$ is the element of the density matrix. The first term in Equation (1) is the standard DFT functional, and the second term is the Hartree-Fock-like interaction, finally the last term corrects for double counting and is given by

$$E_{\mathrm{dc}}[\{n^{\sigma}\}] = \frac{U}{2}n(n-1) - \frac{J}{2}\left[n^{\uparrow}(n^{\uparrow}-1) + n^{\downarrow}(n^{\downarrow}-1)\right] \quad (2)$$

where $n^{\sigma} = \mathrm{Tr}(n^{\sigma}_{mm'})$, with $m(m')$ being the magnetic quantum number, and $n = n^{\uparrow} + n^{\downarrow}$.

## III. RESULTS AND DISCUSSIONS

Strong electronic correlation is a key feature that distinguishes unconventional superconductors including cuprate and nickelate materials from conventional superconductors [46]. However, the nonmagnetic (NM) local density approximation (LDA) band structure is very illuminating and widely discussed in both cuprates and nickelates superconductivity research [21, 47], because the effect of electronic correlation is weakened in the case of optimum doping. As what Damascelli *et al.* found in their angle-resolved photoemission studies (ARPES) of the cuprate superconductors [48], when the system is doped step by step, antiferromagnetic (AFM) correlations are reduced, and a metallic state appears, and eventually (*i.e.*, in the optimum and overdoped regime) the AFM state is destroyed and a large LDA-like Fermi surface emerges. Therefore, the LDA-level study of the electronic structure in our work is designed to reveal the low-energy physics of the metallic state under optimal doping. While the $Ni^{1+\delta}$ valence state in our superlattice arises from interfacial charge transfer and may not represent the exact valence state under optimal doping, LDA provides a reasonable starting point for understanding the electronic behavior in this regime.

*Nonmagnetic electronic structures.*—Unlike the perovskite $NdNiO_3$ ($d^7$-$Ni^{3+}$), which features $NiO_6$ octahedral structures, infinite-layer $NdNiO_2$ ($d^9$-$Ni^{1+}$) exhibits a planar $NiO_2$ layered structure, lacking the corner oxygen atoms, as illustrated in Fig. 1(a). The Fermi surface of $NdNiO_2$ is primarily composed of Ni-$3d_{x^2-y^2}$ and A-site Nd-5*d* orbitals, as shown by the fatbands in Fig. 1(b). This differs from $CaCuO_2$ (Fig. 1(e)), where only the Cu-$3d_{x^2-y^2}$ band crosses the Fermi level, as seen in Fig. 1(f). This distinction may partially explain the relatively low $T_c$ of 15 K in $Nd_{0.8}Sr_{0.2}NiO_2$. Similar to $NdNiO_2$, $SrNiO_2$ ($d^8$-$Ni^{2+}$) also has an infinite-layer structure, as shown in Fig. 1(c), but the bands associated with the A-site Sr atom are far from the Fermi level in Fig. 1(d), simplifying the Fermi surface topology. However, the change in Ni valence state from $Ni^{1+}$ to $Ni^{2+}$ leads to a renormalization of the Ni-3*d* band near the Fermi level. Compared to the band structure of $NdNiO_2$ in Fig. 1(b), $SrNiO_2$ shows a significant increase in the contribution of the Ni-3*d*-$t_{2g}$ orbital to the Fermi surface, yet a cuprate-like Fermi surface with only the Ni-$d_{x^2-y^2}$ orbital occupied is still not achieved. Additionally, as seen from the orbitals-projected density of states (DOSs) in Figs. 1(g-i), the *d*-*p* hybridization is strongest in $CaCuO_2$ for both $t_{2g}$ and $e_g$ orbitals, much weaker in $NdNiO_2$, and intermediate in $SrNiO_2$. Therefore, $SrNiO_2$ presents promising potential for superconductivity design.

To further modulate the Ni-3*d* electron occupancy in $SrNiO_2$, the Mott insulator $LaTiO_3$ (Ti-$3d^1$) was introduced to construct a $(SNO)_1/(LTO)_1$ SL, as shown in Fig. 2(a). The in-plane lattice constant $a$ was matched to the pseudocubic $LaTiO_3$ at 3.938 Å. The GGA band structure of the SL, plotted in Fig. 2(b), reveals fully occupied Ni-$t_{2g}$ and Ni-$d_{3z^2-1}$ orbitals. In addition to the Ni-$d_{x^2-y^2}$ orbital, the Ti-$d_{xy}$ and Ti-$d_{3z^2-1}$ orbitals also significantly contribute to the Fermi surface, primarily around the Γ and A points, functioning similarly to the Nd-5*d* orbitals in $NdNiO_2$ (see Fig.

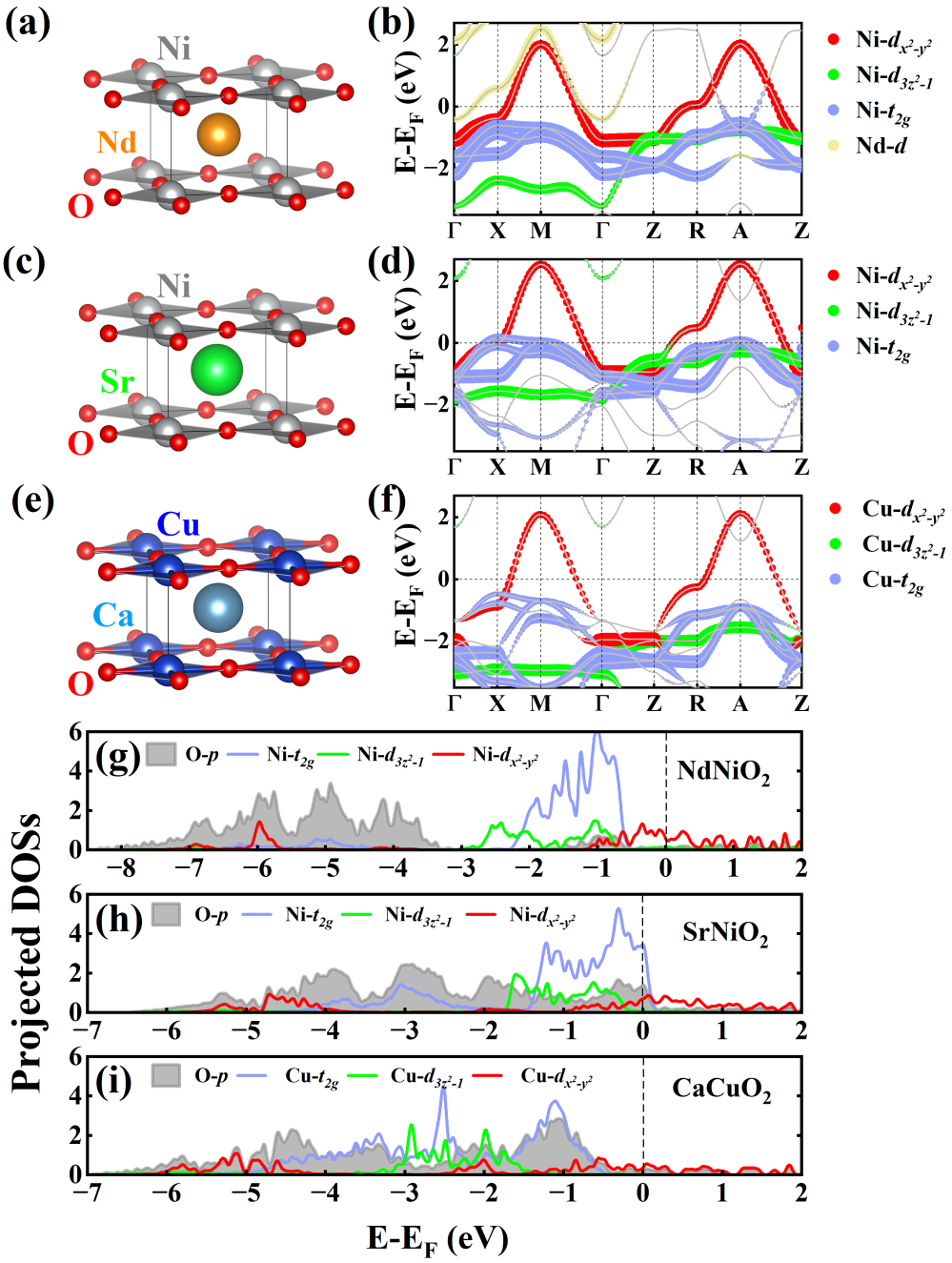


FIG. 1. Schematic crystal structures of (a) $NdNiO_2$, (c) $SrNiO_2$, and (e) $CaCuO_2$. GGA NM band structures of (b) $NdNiO_2$, (d) $SrNiO_2$, and (f) $CaCuO_2$, showing orbital contributions from Ni/Cu-$d_{x^2-y^2}$ (red), Ni/Cu-$d_{3z^2-1}$ (green), Ni/Cu-$t_{2g}$ (lilac), and Nd-$d$ (light yellow). Projected density of states for Ni/Cu-$d_{x^2-y^2}$ (red), Ni/Cu-$d_{3z^2-1}$ (green), Ni/Cu-$t_{2g}$ (lilac), and O-$p$ (grey) in (g) $NdNiO_2$, (h) $SrNiO_2$, and (i) $CaCuO_2$, respectively.

1(b)). Compared to the band structure of $SrNiO_2$ in Fig. 1(d), a clear charge transfer occurs between Ni and Ti, resulting in an electronic reconstruction perpendicular to the interface: $Ni^{2+}/Ti^{3+} \rightarrow Ni^{1+\delta}/Ti^{4-\delta}$ (with $\delta < 1$). This charge transfer is primarily driven by the electronegativity differences [49] between Ni (1.91) and Ti (1.54).

By increasing the number of $SrNiO_2$ layer to 2, as shown in Fig. 2(c), we constructed a bi-layer $(SNO)_2/(LTO)_1$ SL, labeling the $SrNiO_2$ layers as SNO-A and SNO-B. The GGA fatband structures in Figs. 2(d-e) and the orbitals-projected DOSs in Fig. 2(f) reveal a Fermi surface occupied solely by the Ni-$d_{x^2-y^2}$ orbital, with the Ti-3$d$ orbitals fully unoccupied. This indicates an integer charge transfer in the $(SNO)_2/(LTO)_1$ SL: $2Ni^{2+}/Ti^{3+} \rightarrow 2Ni^{1.5+}/Ti^{4+}$. From the Ni-$d_{x^2-y^2}$ fatbands

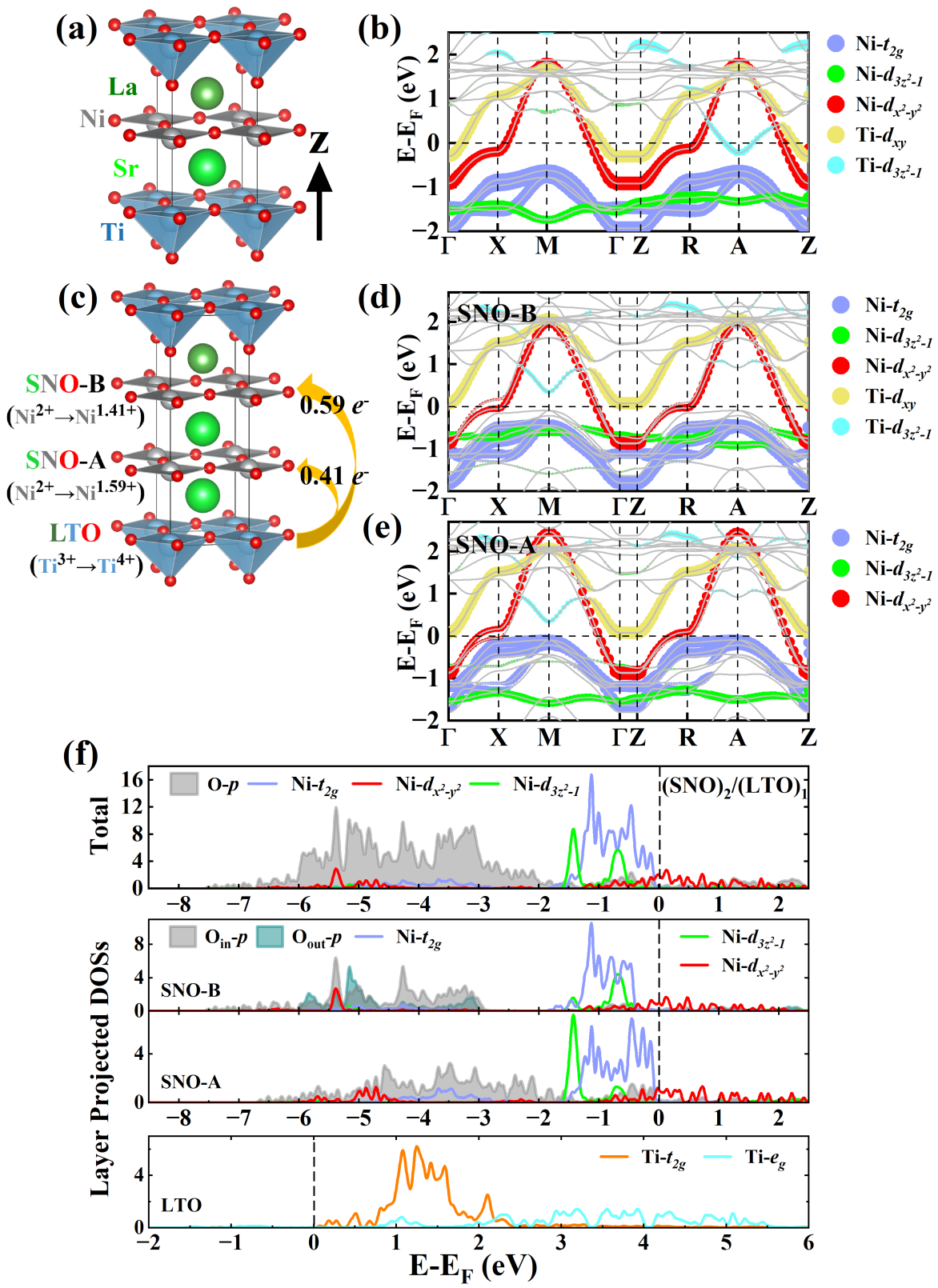


FIG. 2. Schematic geometrical structures of (a) $(SNO)_1/(LTO)_1$ and (c) $(SNO)_2/(LTO)_1$. The inequivalent $NiO_2$ planes are labeled as SNO-A and SNO-B, respectively. (b) GGA NM band structure of $(SNO)_1/(LTO)_1$. GGA fatband structures of $(SNO)_2/(LTO)_1$ for (d) SNO-B and (e) SNO-A. The different orbital contributions are color-coded: Ni-$d_{x^2-y^2}$ (red), Ni-$d_{3z^2-1}$ (green), Ni-$t_{2g}$ (lilac), Ti-$d_{xy}$ (light yellow), and Ti-$d_{3z^2-1}$ (sky blue). (f) Projected DOSs for different orbitals: Ni-$d_{x^2-y^2}$ (red), Ni-$d_{3z^2-1}$ (green), Ni-$t_{2g}$ (lilac), O-$p$ (grey/dark blue), Ti-$t_{2g}$ (orange), and Ti-$e_g$ (sky blue) for $(SNO)_2/(LTO)_1$ and its counterparts: SNO-A, SNO-B, and LTO.

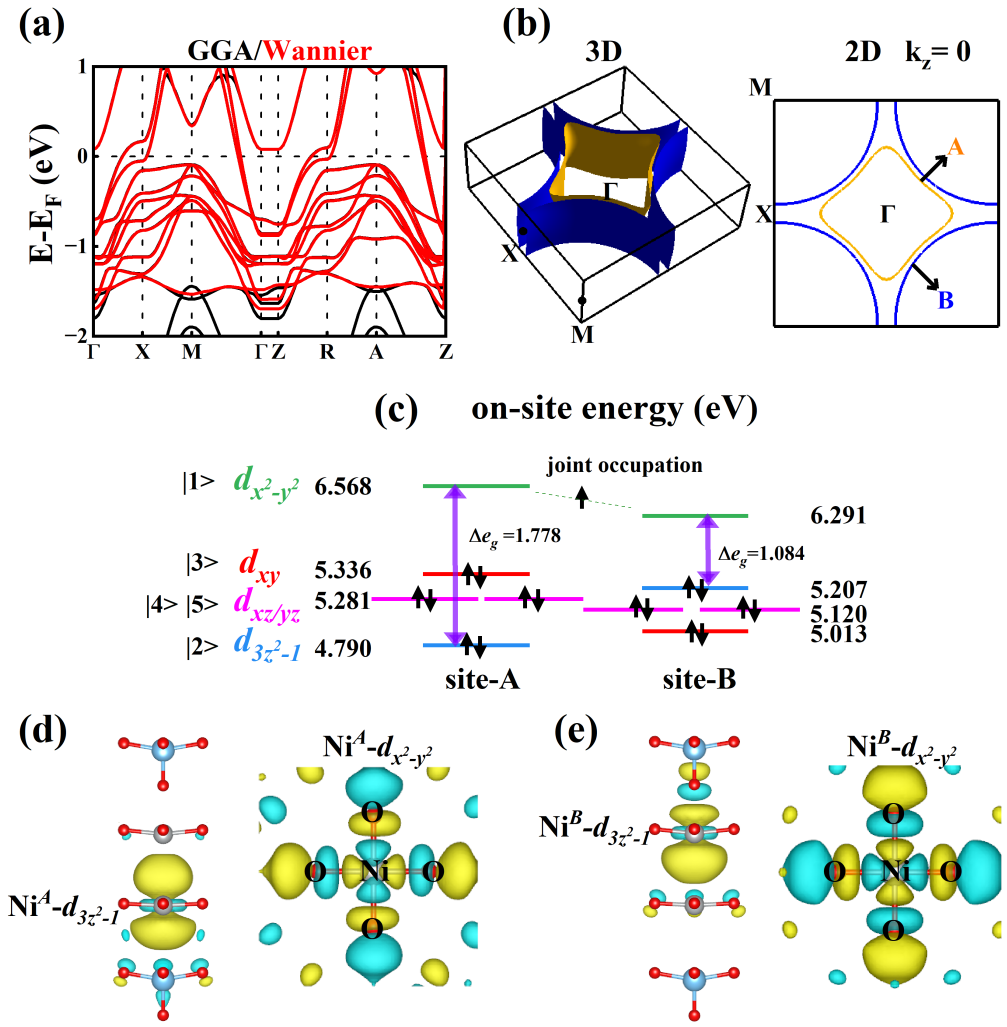


FIG. 3. (a) GGA (black lines) and Wannier (red lines) electronic band structures, and (b) the 3D and 2D Fermi surfaces of $(SNO)_2/(LTO)_1$. In the Fermi surfaces, the two-band feature arises from $Ni^A$-$d_{x^2-y^2}$ (yellow) and $Ni^B$-$d_{x^2-y^2}$ (blue), respectively. (c) On-site energy and electron occupancy of the $Ni^{A/B}$-3$d$ orbitals in $(SNO)_2/(LTO)_1$. (d) and (e) Wannier functions of the $Ni^{A/B}$-$d_{3z^2-1}$ and $Ni^{A/B}$-$d_{x^2-y^2}$ orbitals in $(SNO)_2/(LTO)_1$.

TABLE I. The obtained nearest-neighbor hopping $t_{nm}$ (eV) of Ni-$e_g$ in $(SNO)_2/(LTO)_1$. The parameters of $La_3Ni_2O_7$ at high pressure (HP)[35] and undoped infinite-layer $NdNiO_2$ are also listed for comparison.

| | $e_g$-hopping | $(SrNiO_2)_2/(LaTiO_3)_1$ | $La_3Ni_2O_7$ (HP)[35] | undoped $NdNiO_2$ |
|---|---|---|---|---|
| **Intra-layer** | $t^A_{11}$ | 0.379 | 0.491 | 0.373 |
| | $t^A_{22}$ | 0.013 | 0.115 | 0.027 |
| | $t^A_{12}$ | 0.034 | 0.240 | 0.021 |
| | $t^B_{11}$ | 0.322 | | |
| | $t^B_{22}$ | 0.006 | | |
| | $t^B_{12}$ | 0.061 | | |
| **Inter-layer** | $t^{AB}_{22}$ | 0.309 | 0.644 | 0.323 |
| | $t^{AB}_{11}$ | 0.014 | <0.01 | 0.028 |

for SNO-A and SNO-B in Figs. 2(d-e) and their corresponding DOSs in Fig. 2(f), we infer that SNO-B receives more electrons from Ti than SNO-A during charge transfer. By integrating the DOS, the estimated electron occupancy for the Ni-$d_{x^2-y^2}$ orbital is 0.59 for SNO-B ($Ni^{1.41+}$) and 0.41 for SNO-A ($Ni^{1.59+}$). Additionally, from the distribution of oxygen $p$-bands in Fig. 2(f), it is evident that the $d$-$p$ hybridization is weaker than in $SrNiO_2$ (Fig. 1(h)), but stronger compared to $NdNiO_2$ (Fig. 1(g)).

*Wannierization.*—To better understand the microscopic Ni-3$d$ orbital physics of bi-layer $(SNO)_2/(LTO)_1$ SL, we extracted model hamiltonian parameters by MLWFs downfolding technique, based on the above parameter-free GGA density functional simulations. Fourier transformation of the orthonormalized MLWF Hamiltonian $H(k)$ yields on-site energies and hopping integrals, denoted as

$$H_{\mathbf{0}n,\mathbf{R}m} \equiv \langle \mathbf{0}n|H|\mathbf{R}m\rangle \equiv t^{\mathbf{R}}_{nm}$$

in a Wannier representation. Here, $|\mathbf{0}n\rangle$ is MLWF Wannier function in home cell associated with band $n$, and $|\mathbf{R}m\rangle$ is orthonormal MLWF Wannier function in cell $\mathbf{R}$ associated with band $m$. As a result, the tight-binding model Hamiltonian can be written as follows:

$$H(\mathbf{k}) = \sum_n \varepsilon_n c^\dagger_{\mathbf{0}n} c_{\mathbf{0}n} + \sum_{\mathbf{R}nm} \left( t^{\mathbf{R}}_{nm} e^{i\mathbf{k}\cdot\mathbf{R}} c^\dagger_{\mathbf{0}n} c_{\mathbf{R}m} + \text{H.c.} \right) \quad (3)$$

where $\varepsilon_n$ is the on-site energies of the orbitals. $c_{\mathbf{0}n}(c^\dagger_{\mathbf{0}n})$ and $c_{\mathbf{R}m}(c^\dagger_{\mathbf{R}m})$ denote the annihilation (creation) operators of electrons.

Given that the interfacial Ti-$d_{xy}$ and Ti-$d_{3z^2-1}$ bands are relatively close to the Fermi level, we chose to downfold a 12-band Hamiltonian to describe the key orbitals: $|1\rangle$ = Ni-$d_{x^2-y^2}$, $|2\rangle$ = Ni-$d_{3z^2-1}$, $|3\rangle$ = Ni-$d_{xy}$, $|4\rangle$ = Ni-$d_{xz}$, $|5\rangle$ = Ni-$d_{yz}$ from the two SNO layers, and the Ti-$d_{xy}$ and Ti-$d_{3z^2-1}$ orbitals from the LTO layer. The essential physics can be captured with the derived parameters, such as on-site energies, the $e_g$ crystal field splitting energy $\Delta_{e_g} = \varepsilon_{x^2-y^2} - \varepsilon_{3z^2-1}$, and the direct Ni–Ni $e_g$ hopping $t_{nm}$. The extracted values are shown in Fig. 3(c) and Table I, with the corresponding interpolated band structure and Fermi surfaces presented in Figs. 3(a) and 3(b). For comparison, the parameters for the high-pressure superconducting phase of $La_3Ni_2O_7$ and undoped infinite-layer $NdNiO_2$ are also listed in Table I.

In Fig. 3(a), the resulting tight-binding energy bands show well agreement with the first-principles bands. Both the 3D Fermi surface and the 2D projection at the $k_z = 0$ plane in Fig. 3(b) reveal crossings of two Ni-$d_{x^2-y^2}$ bands from the SNO-A and SNO-B layers. The Fermi surface of SNO-B exhibits a cuprate-like bulging toward the Γ point [47], while the SNO-A Fermi surface forms an electron pocket around the Γ point. This purely Ni-$d_{x^2-y^2}$-occupied double-band Fermi surface closely resembles that of the recently discovered high-pressure superconducting $La_3Ni_2O_7$, with the notable difference being the small participation from Ni-$d_{3z^2-1}$ is excluded now.

In the $(SNO)_2/(LTO)_1$ SL, the two SNO layers at the interface exhibit distinct Ni-O coordination environments: planar

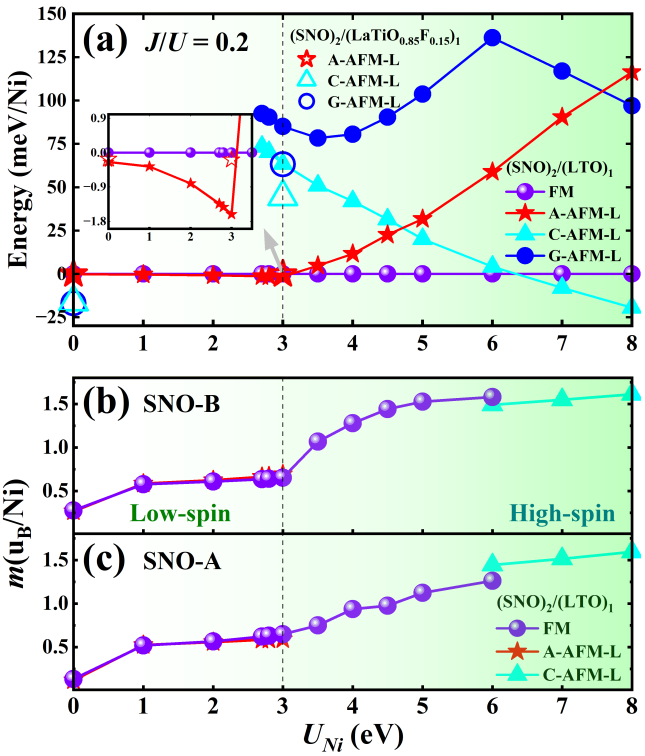


FIG. 4. (a) The calculated GGA+$U$ total energies and (b) the spin moment per Ni atom as a function of $U_{Ni}$ for different magnetic configurations in the $(SNO)_2/(LTO)_1$ SL. The ratio $J/U$ is set to 0.2, with the total energy of the FM state used as the reference. The inset in (a) shows the enlarged energy difference between the A-AFM-L and FM states as $U_{Ni}$ varies from 0 to 3.5 eV. The calculated result for $(SNO_{0.85}F_{0.15})_2/(LTO)_1$ SL at $U_{Ni}$ = 0, 3 eV (big open symbol) is also included in (a) and its inset.

square for SNO-A and square pyramidal for SNO-B, leading to different $d$-orbital crystal field splittings, as shown in Fig. 3(c). The orbital configurations derived from the tight-binding on-site energies in Fig. 3(c) are consistent with the first-principles electronic structure results in Figs. 2(d-f). The crystal field splitting $\Delta e_g$ for $Ni^A$ is 0.7 eV larger than that for $Ni^B$. Both $Ni^{A/B}$-$t_{2g}$ and $Ni^{A/B}$-$d_{3z^2-1}$ orbitals are fully occupied, while the $Ni^A$-$d_{x^2-y^2}$ and $Ni^B$-$d_{x^2-y^2}$ orbitals share one electron between them. The Ni-$e_g$ hopping integrals (see Table I) of the $(SNO)_2/(LTO)_1$ SL are comparable to those of undoped infinite-layer $NdNiO_2$, although they are generally smaller than those in $La_3Ni_2O_7$, which is expected due to the structural differences under high pressure. In Figs. 3(d-e), we present the disentangled Wannier functions for the $Ni^{A/B}$-$e_g$ orbitals in the $(SNO)_2/(LTO)_1$ SL. The $Ni^{A/B}$-$d_{x^2-y^2}$ orbitals exhibit $p$-$d$ covalent hybridization, similar to $La_3Ni_2O_7$ [35], while the $Ni^{A/B}$-$d_{3z^2-1}$ orbitals are more localized due to the absence of apical oxygen atoms linking the two Ni-$d_{3z^2-1}$ orbitals.

*Magnetism.*—To investigate the magnetic properties of the $(SNO)_2/(LTO)_1$ SL, we carried out the DFT GGA+$U$ calculations with $J/U = 0.2$ for Ni-3$d$. Unlike the strong AFM fluctuations observed in cuprates, no long-range magnetic order

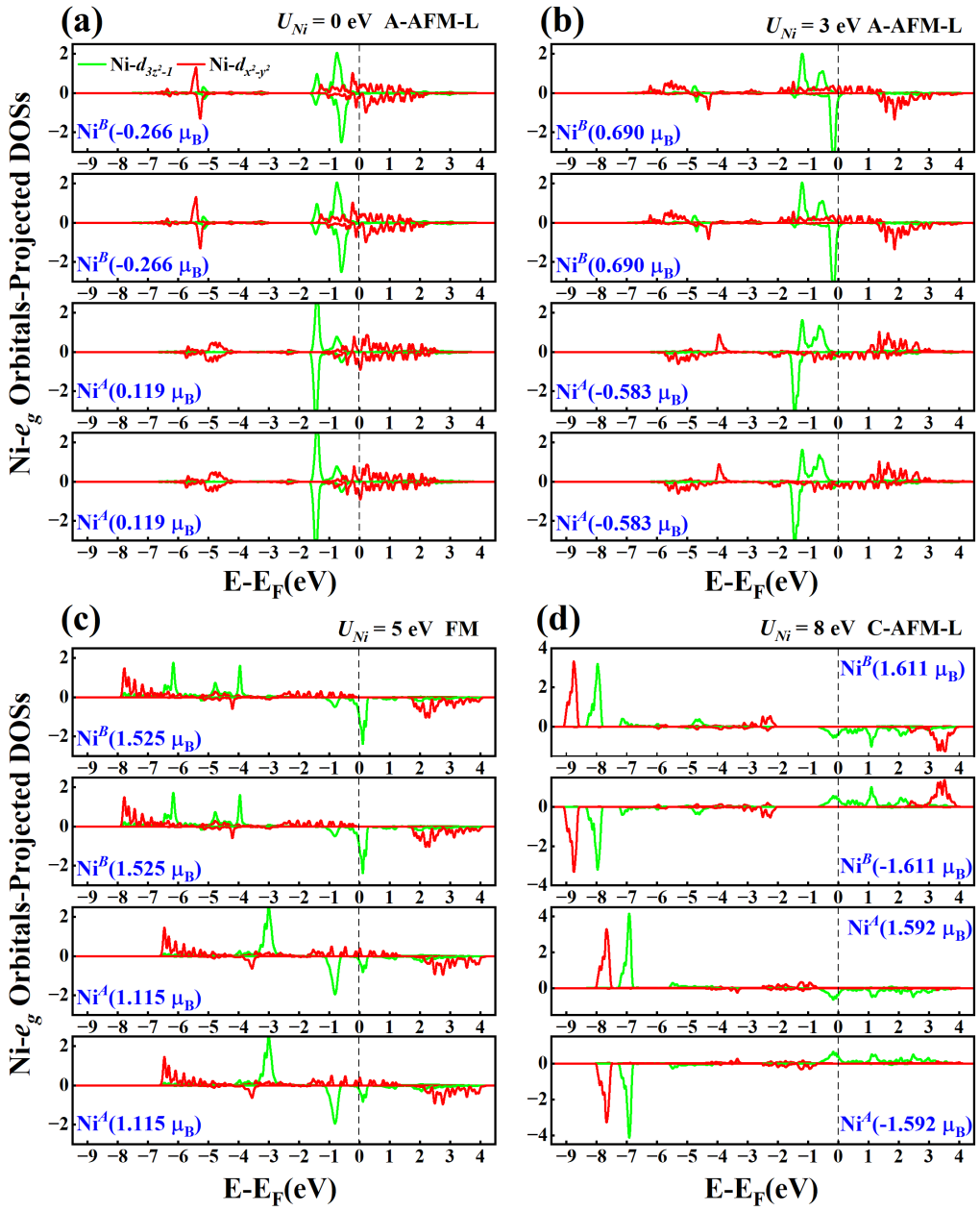


FIG. 5. GGA+$U$ spin-polarized Ni$^{A/B}$-$e_g$ orbital-projected DOSs for the $(SNO)_2/(LTO)_1$ SL: Ni$^{A/B}$-$d_{x^2-y^2}$ (red) and Ni$^{A/B}$-$d_{3z^2-1}$ (green), calculated for different magnetic ground states at $U_{Ni}$ = 0, 3, 5, and 8 eV (with $U_{Ti}$ = 4 eV fixed).

has been found in $La_3Ni_2O_7$, whereas local AFM correlations have been experimentally reported in infinite-layer $NdNiO_2$ [14]. Due to the complexity of magnetic coupling in nickelates, we introduced a range of $U$ values on Ni-3$d$ (with $U_{Ti}$= 4 eV fixed) to explore possible magnetic coupling trends in our Ni-based superlattice. The calculated total energies of various magnetic states, along with their corresponding magnetic moments arising from the spin and orbital configurations, are shown in Figs. 4(a) and 4(b-c). The spin-polarized Ni$^{A/B}$-$e_g$ orbital-projected DOSs for different magnetic ground states at $U$= 0, 3, 5 and 8 eV (with $U_{Ti}$ = 4 eV) are shown in Fig. 5. Since the SNO-A and SNO-B layers differ in local chemical structure and crystal field environment, the two out-of-plane Ni atoms are inequivalent, leading to different valence states and magnetic moments. We find that the C-type and G-type antiferromagnetic-like (AFM-L) states are highly unstable at small $U$ values, converging to other magnetic states. As $U$ increases beyond 3 eV, the energy of the G-AFM-L state rises, while that of the C-AFM-L state keeps decreasing. In Fig. 4(a), when $U \leq 3$ eV, the A-AFM-L state is slightly lower in energy than the FM state, with a maximum energy difference of 1.62 meV/Ni at $U = 3$ eV, indicating weak interlayer AFM coupling. A similar result has been observed in $La_3Ni_2O_7$ [35] and $NdNiO_2$ [23]. However, we observe intralayer FM

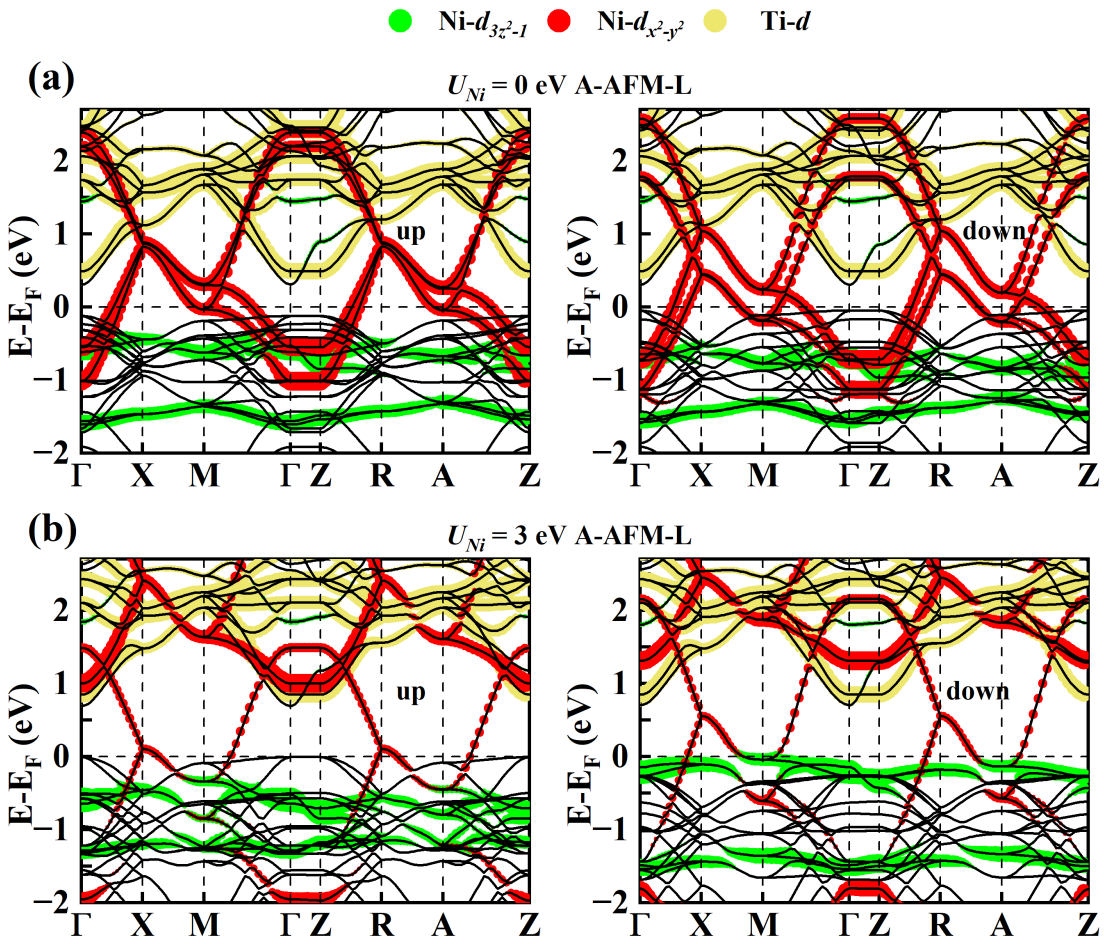


FIG. 6. GGA+$U$ spin-polarized band structures for the $(SNO)_2/(LTO)_1$ SL, calculated for different magnetic ground states at $U_{Ni}$ = 0 and 3 eV (with $U_{Ti}$ = 4 eV fixed). The different orbital contributions are color-coded: Ni-$d_{x^2-y^2}$ (red), Ni-$d_{3z^2-1}$ (green), and Ti-3$d$ (light yellow).

coupling by comparing the energy difference between the C-AFM-L and FM states, which contrasts with the AFM coupling found in $La_3Ni_2O_7$ and $NdNiO_2$. At $U = 3$ eV, the $e_g$ orbital occupation of the A-AFM-L state is qualitatively similar to that at $U = 0$ eV, with the only difference being enhanced spin splitting, as seen in the orbitals-projected DOSs in Figs. 5(a-b). Hund's rule states that electrons prefer to maximize their total spin by occupying separate orbitals with parallel spins before pairing, leading to high-spin configurations. As $U$ increases, the electron-electron repulsion becomes stronger, making double occupancy within the same orbital more energetically unfavorable. Since Hund's coupling favors high-spin configurations, electrons tend to distribute across different orbitals to minimize pairing. This results in orbital polarization, where single electrons preferentially occupy different orbitals. Consequently, as $U$ increases, Hund's coupling stabilizes distinct orbital occupations, giving rise to different orbital ordering. For $3 < U \leq 6$ eV, the system undergoes a magnetic transition to a FM ground state. Simultaneously, a charge redistribution occurs between the two $e_g$ orbitals, with the Ni-$d_{x^2-y^2}$ orbital gaining electrons from the Ni-$d_{3z^2-1}$ orbital (see Fig. 5(c)), and the SL gradually transitions to a high-spin state. Ultimately, when $U > 6$ eV, the C-AFM-L high-spin state becomes the ground state, as shown in Fig. 5(d).

In general, the energy evolution of the A-type and C-type AFM-L states, along with the FM state, shows that the weak interlayer AFM exchange coupling disappears around $U = 3$ eV, after which FM coupling strengthens with increasing $U$. However, the intralayer FM exchange coupling weakens and eventually reverses when $U$ exceeds 6 eV. It is worth noting that $La_3Ni_2O_7$ exhibits a paramagnetic metallic ground state at $U = 0$ eV, with nonzero $U$ values in the literature typically ranging from 3.5 to 4.3 eV [24, 50, 51] to get magnetic ground state. However, the $(SNO)_2/(LTO)_1$ SL remains a spin-polarized magnetic metal even at $U = 0$ eV, with its magnetic ground state properties remaining stable up to $U = 3$ eV, a value typically applied for elemental nickel. Thus, the $e_g$ orbital reconstruction and high-spin state driven by crystal field splitting and increasing $U$ (> 3 eV) and $J$ appear less reasonable in this case. For comparison with the NM GGA band structures in Figs. 2d–2e, we present the spin-polarized GGA+$U$ band structures of the A-AFM-L magnetic ground state at reasonable $U$= 0, 3 eV (with $U_{Ti}$ = 4 eV) in Fig. 6. As $U$ increases, the Ti-3$d$ states (light yellow) remain in the

conduction band, indicating that the Ti-3$d$ orbitals are unoccupied and the Ti valence state remains +4. This is in excellent agreement with the NM GGA results and confirms that the full charge transfer from Ti to Ni is robust and independent of correlation effects.

Additionally, we observe magnetic instability when $U \leq 3$ eV, which arises from the degenerate magnetic ground states with nearly equal total energies for the FM and A-AFM-L states. A similar instability has been reported in $La_3Ni_2O_7$ [35]. Experimentally, it is quite challenging to observe large-scale ordered AFM states in nickelates with superconductivity, in contrast to the long-range, stable AFM order found in cuprates. However, the intralayer FM coupling at small $U$ values is inconsistent with the intended superconducting design. This discrepancy is likely due to the deviation of the $Ni^{A/B}$ valence states ($Ni^{1.59+}$/$Ni^{1.41+}$) from the $Ni^{1.2+}$ found in superconducting $Nd_{0.8}Sr_{0.2}NiO_2$ or the $Ni^{1+}$ in undoped $NdNiO_2$. To test this hypothesis, we fine-tuned the average valence state of Ni to $Ni^{1.2+}$ by doping F atoms in $NiO_2$ double layers at a concentration of 0.15, resulting in the $(SNO_{0.85}F_{0.15})_2$/$(LTO)_1$ SL. This modification can be experimentally achieved by controlling oxygen pressure during preparation process. We find that F doping effectively reduces both the interlayer AFM and intralayer FM couplings at $U = 3$ eV, from 1.62 meV and 63.47 meV to 0.19 meV and 44.42 meV per Ni, respectively, as shown by the big open symbols in Fig. 4(a). Interestingly, at $U = 0$ eV, the G-AFM-L and C-AFM-L states emerge as the most stable magnetic ground states, with nearly degenerate energies that are 16.96 meV and 16.18 meV per Ni, respectively, lower than that of the FM state.

## IV. CONCLUSIONS

Our comprehensive theoretical study explores $(SNO)_n$/$(LTO)_1$ SLs to elucidate their electronic and magnetic properties. We uncover a complete integer charge transfer: $2Ni^{2+}/Ti^{3+} \rightarrow (Ni^{1.41+}+Ni^{1.59+})/Ti^{4+}$ at the interfaces of $(SNO)_2$/$(LTO)_1$, which refines the Fermi surface from multi-orbital contributions to a purely Ni-$d_{x^2-y^2}$ orbital character. The key features of Ni-$d_{x^2-y^2}$ orbital occupation, electronic properties, and the Fermi surface show a resemblance to superconducting cuprates and high-pressure $La_3Ni_2O_7$. The nearest-neighbor $e_g$ hopping parameters are closely aligned with those in infinite-layer $NdNiO_2$, though smaller than those found in high-pressure $La_3Ni_2O_7$. In contrast to $NdNiO_2$, factors that limit transition temperatures (15 K), such as 5$d$-3$d$ hybridization, self-doping between Nd and Ni atoms, and weak $p$-$d$ hybridization, have been either completely suppressed or improved in our SL system. Our magnetic state calculations indicate that the system is in a low-spin state with magnetic instability at a reasonable correlation $U$ value of 1 to 3 eV, similar to what is observed in $La_3Ni_2O_7$. The magnetic coupling is highly sensitive to the valence state of Ni atoms and can be fine-tuned by F-doping in $NiO_2$ double layers to simulate an oxygen pressure environment during the preparation process. These findings not only underscore the promising high-$T_c$ superconductivity of nickelate heterostructures at ambient pressure, but also enhance our comprehension of the complex superconducting behaviors exhibited by nickelate materials.

While our study theoretically constructs a $(SNO)_2$/$(LTO)_1$ superlattice, its experimental realization is feasible based on existing thin-film growth techniques such as pulsed laser deposition (PLD) and molecular beam epitaxy (MBE), combined with $CaH_2$ chemical reduction. These methods have been successfully applied to the fabrication of oxide heterostructures [4, 14, 29–32]. Additionally, previous experimental studies on $LaNiO_3$/$LaTiO_3$ superlattices [52] further support the viability of such nickelate-titanate heterostructures. These considerations suggest that the proposed superlattice could be experimentally realized, provided that suitable growth conditions are carefully optimized.

## V. ACKNOWLEDGMENTS

X.Y. would like to acknowledge financial support from the National Key Research and Development Program of China (Grant Nos. 2021YFA1600204), the National Natural Science Foundation of China (NSFC) (Grant No. 12174397).

[1] J. G. Bednorz and K. A. Müller, Possible high $T_c$ superconductivity in the Ba-La-Cu-O system, Zeitschrift für Physik B Condensed Matter **64**, 189-193 (1986).

[2] B. Cheng, D. Cheng, K. Lee, L. Luo, Z. Chen, Y. Lee, B. Y. Wang, M. Mootz, I. E. Perakis, Z.-X. Shen, H. Y. Huang, J. Wang, Evidence for $d$-wave superconductivity of infinite-layer nickelates from low-energy electrodynamics, Nature Materials **23**, 775-781 (2024).

[3] C. T. Parzyck, N. K. Gupta, Y. Wu, V. Anil, L. Bhatt, M. Bouliane, R. Gong, B. Z. Gregory, A. Luo, R. Sutarto, F. He, Y. -D. Chuang, T. Zhou, G. Herranz, L. T-. Kourkoutis, A. singer, D. G. Schlom, D.G. Hawthorn, K.M.Shen, Absence of $3a_0$ charge density wave order in the infinite-layer nickelate $NdNiO_2$, Nature Materials **23**, 486-491 (2024).

[4] D. Li, K. Lee, B. Y. Wang, M. Osada, S. Crossley, H. R. Lee, Y. Cui, Y. Hikita, H. Y. Hwang, Superconductivity in an infinite-layer nickelate, Nature **572**, 624-627 (2019).

[5] L.-H. Hu and C. Wu, Two-band model for magnetism and superconductivity in nickelates, Physical Review Research **1**, 032046 (2019).

[6] E. Been, W.-S. Lee, H. Y. Hwang, Y. Cui, J. Zaanen, T. Devereaux, B. Moritz, C. Jia, Electronic structure trends across the rare-earth series in superconducting infinite-layer nickelates, Physical Review X **11**, 011050 (2021).

[7] F. Lechermann, Late transition metal oxides with infinite-layer structure: Nickelates versus cuprates, Physical Review B **101**, 081110 (2020).

[8] M. Hepting, D. Li, C. J. Jia, H. Lu, E. Paris, Y. Tseng, X. Feng, M. Osada, E. Been, Y. Hikita, Y. -D.Chuang, Z. Hussain, K. J. Zhou, A. Nag, M. Garcia-Fernandez, M. Rossi, H. Y. Huang, D. J. Huang, Z. X. Shen, T. Schmitt, H. Y. Hwang, B. Moritz, J. Zaanen, T. P. Devereaux, W. S. Lee, Electronic structure of the parent compound of superconducting infinite-layer nickelates, Nature Materials **19**, 381-385 (2020).

[9] V. I. Anisimov, D. Bukhvalov, and T. M. Rice, Electronic structure of possible nickelate analogs to the cuprates, Physical Review B **59**, 7901 (1999).

[10] G. A. Pan, D. F. Segedin, H. LaBollita, Q. Song, E. M. Nica, B. H. Goodge, A. T. Pierce, S. Doyle, S. Novakov, D. Córdova Carrizales, A. T. N'Diaye, P. Shafer, H. Paik, J. T. Heron, J. A. Mason, A. Yacoby, L. F. Kourkoutis, O. Erten, C. M. Brooks, A. S. Botana, J. A. Mundy, Superconductivity in a quintuple-layer square-planar nickelate, Nature Materials **21**, 160-164 (2022).

[11] J. Chaloupka and G. Khaliullin, Orbital order and possible superconductivity in $LaNiO_3/LaMO_3$ superlattices, Physical Review Letters **100**, 016404 (2008).

[12] H. Guo, Z. W. Li, L. Zhao, Z. Hu, C. F. Chang, C.-Y. Kuo, W. Schmidt, A. Piovano, T. W. Pi, O. Sobolev, D. I. Khomskii, L. H. Tjeng, A. C. Komarek, Antiferromagnetic correlations in the metallic strongly correlated transition metal oxide $LaNiO_3$, Nature Communications **9**, 43 (2018).

[13] K.-W. Lee and W. E. Pickett, Infinite-layer $LaNiO_2$: $Ni^{1+}$ is not $Cu^{2+}$, Physical Review B **70**, 165109 (2004).

[14] X. Yang, M. Li, Z. Ding, L. Li, C. Ji, G. Wu, Review on Developments and Progress in Nickelate-Based Heterostructure Composites and Superconducting Thin Films, Advanced Quantum Technologies **6**, 2200065 (2023).

[15] C. Ji, G. Wu, S. Yang, G. Wu, X. Yang, Completely polarized $e_g$ orbitals realized in $d^7$-$Ni^{3+}$ based heterointerface, Physical Review Materials **4**, 124804 (2020).

[16] P. Hansmann, X. Yang, A. Toschi, G. Khaliullin, O. K. Andersen, K. Held, Turning a nickelate Fermi surface into a cupratelike one through heterostructuring, Physical Review Letters **103**, 016401 (2009).

[17] P. Hansmann, A. Toschi, X. Yang, O. K. Andersen, K. Held, Electronic structure of nickelates: From two-dimensional heterostructures to three-dimensional bulk materials, Physical Review B **82**, 235123 (2010).

[18] N. N. Wang, M. W. Yang, Z. Yang, K. Y. Chen, H. Zhang, Q. H. Zhang, Z. H. Zhu, Y. Uwatoko, L. Gu, X. L. Dong, J. P. Sun, K. J. Jin, J.-G. Cheng, Pressure-induced monotonic enhancement of $T_c$ to over 30 K in superconducting $Pr_{0.82}Sr_{0.18}NiO_2$ thin films, Nature Communications **13**, 4367 (2022).

[19] W. L. McMillan, Transition temperature of strong-coupled superconductors, Physical Review **167**, 331-344 (1968).

[20] H. Sakakibara, H. Usui, K. Suzuki, T. Kotani, H. Aoki, K. Kuroki, Model construction and a possibility of cupratelike pairing in a new $d^9$ nickelate superconductor (Nd,Sr)$NiO_2$, Physical Review Letters **125**, 077003 (2020).

[21] A. S. Botana, M. R. Norman, Similarities and differences between $LaNiO_2$ and $CaCuO_2$ and implications for superconductivity, Physical Review X **10**, 011024 (2020).

[22] R. Zhang, C. Lane, B. Singh, J. Nokelainen, B. Barbiellini, R. S. Markiewicz, A. Bansil, J. Sun, Magnetic and $f$-electron effects in $LaNiO_2$ and $NdNiO_2$ nickelates with cuprate-like $3d_{x^2-y^2}$ band, Communications Physics **4**, 118 (2021).

[23] S. Ryee, H. Yoon, T. J. Kim, M. Y. Jeong, M. J. Han, Induced magnetic two-dimensionality by hole doping in the superconducting infinite-layer nickelate $Nd_{1-x}Sr_xNiO_2$, Physical Review B **101**, 064513 (2020).

[24] H. Sun, M. Huo, X. Hu, J. Li, Z. Liu, Y. Han, L. Tang, Z. Mao, P. Yang, B. Wang, J. Cheng, D.-X. Yao, G.-M. Zhang, M. Wang, Signatures of superconductivity near 80 $K$ in a nickelate under high pressure, Nature **621**, 493-498 (2023).

[25] D.-K. Seo, W. Liang, M.-H. Whangbo, Z. Zhang, M. Greenblatt, Electronic band structure and Madelung potential study of the Nickelates $La_2NiO_4$, $La_3Ni_2O_7$, and $La_4Ni_3O_{10}$, Inorganic Chemistry **35**, 6396-6400 (1996).

[26] G. Wu, J. J. Neumeier, M. F. Hundley, Magnetic susceptibility, heat capacity, and pressure dependence of the electrical resistivity of $La_3Ni_2O_7$ and $La_4Ni_3O_{10}$, Physical Review B **63**, 245120 (2001).

[27] X.-Z. Qu, D.-W. Qu, J. Chen, C. Wu, F. Yang, W. Li, G. Su, Bilayer $t$-$J$-$J_\perp$ Model and Magnetically Mediated Pairing in the Pressurized Nickelate $La_3Ni_2O_7$, Physical Review Letters **132**, 036502 (2024).

[28] R. Jiang, J. Hou, Z. Fan, Z.-J. Lang, W. Ku, Pressure Driven Fractionalization of Ionic Spins Results in Cupratelike High-$T_c$ Superconductivity in $La_3Ni_2O_7$, Physical Review Letters **132**, 126503 (2024).

[29] A. D. Caviglia, S. Gariglio, N. Reyren, D. Jaccard, T. Schneider, M. Gabay, S. Thiel, G. Hammerl, J. Mannhart, J.-M. Triscone, Electric field control of the $LaAlO_3/SrTiO_3$ interface ground state, Nature **456**, 624-627 (2008).

[30] A. Ohtomo and H. Y. Hwang, A high-mobility electron gas at the $LaAlO_3/SrTiO_3$ heterointerface, Nature **427**, 423-426 (2004).

[31] F. Bi, M. Huang, S. Ryu, H. Lee, C.-W. Bark, C.-B. Eom, P. Irvin, J. Levy, Room-temperature electronically-controlled ferromagnetism at the $LaAlO_3/SrTiO_3$ interface, Nature Communications **5**, 5019 (2014).

[32] S. Thiel, G. Hammerl, A. Schmehl, C. W. Schneider, J. Mannhart, Tunable quasi-two-dimensional electron gases in oxide heterostructures, Science **313**, 1942-1945 (2006).

[33] X. Yang, H. Su, Electronic reconstruction and surface two-dimensional electron gas in a polarized heterostructure with a hole-doped single copper-oxygen plane, Physical Review B **87**, 205116 (2013).

[34] X. Yang, H. Su, Polarization and Electric Field Dependence of Electronic Properties in $LaAlO_3/SrTiO_3$ Heterostructures, ACS Applied Materials & Interfaces **3**(10), 3819-3823 (2011).

[35] Y. Zhang, L.-F. Lin, A. Moreo, E. Dagotto, Electronic structure, dimer physics, orbital-selective behavior, and magnetic tendencies in the bilayer nickelate superconductor $La_3Ni_2O_7$ under pressure, Physical Review B **108**, L180510 (2023).

[36] G. Kresse, D. Joubert, From ultrasoft pseudopotentials to the projector augmented-wave method, Physical Review B **59**, 1758-1775 (1999).

[37] P. E. Blöchl, Projector augmented-wave method, Physical Review B **50**, 17953-17979 (1994).

[38] G. Kresse, J. Hafner, *Ab initio* molecular dynamics for liquid metals, Physical Review B **47**, 558-561 (1993).

[39] G. Kresse, J. Hafner, *Ab initio* molecular-dynamics simulation of the liquid-metal–amorphous-semiconductor transition in germanium, Physical Review B **49**, 14251-14269 (1994).

[40] J. P. Perdew, K. Burke, M. Ernzerhof, Generalized Gradient Approximation Made Simple, Physical Review Letters **77**, 3865-3868 (1996).

[41] G. Kresse, J. Furthmüller, Efficient iterative schemes for *ab initio* total-energy calculations using a plane-wave basis set, Physical Review B **54**, 11169-11186 (1996).

[42] G. Kresse, J. Furthmüller, Efficiency of *ab-initio* total energy calculations for metals and semiconductors using a plane-wave basis set, Computational Materials Science **6**, 15-50 (1996).

[43] A. I. Liechtenstein, V. I. Anisimov, J. Zaanen, Density-functional theory and strong interactions: Orbital ordering in Mott-Hubbard insulators, Physical Review B **52**, R5467 (1995).

[44] N. Marzari, D. Vanderbilt, Maximally localized generalized Wannier functions for composite energy bands, Physical Review B **56**, 12847 (1997).

[45] A. A. Mostofi, J. R. Yates, Y.-S. Lee, I. Souza, D. Vanderbilt, N. Marzari, Wannier90: A tool for obtaining maximally-localised Wannier functions, Computer Physics Communications **178**, 685-699 (2008).

[46] G. Kotliar, S. Y. Savrasov, K. Haule, V. S. Oudovenko, O. Parcollet, C. A. Marianetti, Electronic structure calculations with dynamical mean-field theory, Rev. Mod. Phys. **78**, 865 (2006).

[47] O. K. Andersen, A. I. Liechtenstein, O. Jepsen, F. Paulsen, LDA energy bands, low-energy hamiltonians, $t'$, $t''$, $t_\perp(k)$, and $J_\perp$, Journal of Physics and Chemistry of Solids **56**, 1573-1591 (1995).

[48] A. Damascelli, Z. Hussain, Z. X. Shen, Angle-resolved photoemission studies of the cuprate superconductors, Rev. Mod. Phys. **75**, 473 (2003).

[49] H. Chen and A. Millis, Charge transfer driven emergent phenomena in oxide heterostructures, Journal of Physics: Condensed Matter **29**,243001 (2017).

[50] H. LaBollita, V. Pardo, M. R. Norman, A. S. Botana, Electronic structure and magnetic properties of $La_3Ni_2O_7$ under pressure : active role of the Ni-$d_{x^2-y^2}$ orbitals, arXiv:2309.17279

[51] V. V. Poltavets, K. A. Lokshin, A. H. Nevidomskyy, M. Croft, T. A. Tyson, J. Hadermann, G. Van Tendeloo, T. Egami, G. Kotliar, N. ApRoberts-Warren, A. P. Dioguardi, N. J. Curro, M. Greenblatt, Bulk Magnetic Order in a Two-Dimensional $Ni^{1+}/Ni^{2+}$ ($d^9/d^8$) Nickelate, Isoelectronic with Superconducting Cuprates, Physical Review Letters **104**, 206403 (2010).

[52] Ankit S. Disa, Divine P. Kumah, Andrei Malashevich, Hanghui Chen, Dario A. Arena, Eliot D. Specht, Sohrab Ismail-Beigi, F. J. Walker, Charles H. Ahn, Orbital Engineering in Symmetry-Breaking Polar Heterostructures, Physical Review Letters **114**, 026801 (2015).